

The use of 6DOF measurement in volcano seismology – A first application to Stromboli volcano

J. Wassermann, T. Braun, M. Ripepe, F. Bernauer, F. Guattari, H. Igel



PII: S0377-0273(22)00030-0

DOI: <https://doi.org/10.1016/j.jvolgeores.2022.107499>

Reference: VOLGEO 107499

To appear in: *Journal of Volcanology and Geothermal Research*

Received date: 28 July 2021

Revised date: 16 January 2022

Accepted date: 5 February 2022

Please cite this article as: J. Wassermann, T. Braun, M. Ripepe, et al., The use of 6DOF measurement in volcano seismology – A first application to Stromboli volcano, *Journal of Volcanology and Geothermal Research* (2021), <https://doi.org/10.1016/j.jvolgeores.2022.107499>

This is a PDF file of an article that has undergone enhancements after acceptance, such as the addition of a cover page and metadata, and formatting for readability, but it is not yet the definitive version of record. This version will undergo additional copyediting, typesetting and review before it is published in its final form, but we are providing this version to give early visibility of the article. Please note that, during the production process, errors may be discovered which could affect the content, and all legal disclaimers that apply to the journal pertain.

The Use of 6DOF Measurement in Volcano Seismology – a First Application to Stromboli Volcano

J. Wassermann¹, T. Braun², M. Ripepe³, F. Bernauer¹, F. Guattari⁴ and H. Igel¹

¹Department of Earth and Environmental Sciences, LMU Munich, Germany.

²National Institute of Geophysics and Volcanology (INGV), Arezzo Observatory, Italy.

³Department of Earth Science of the University of Florence, Italy

⁴iXblue, St-Germain-en-Laye, France.

Corresponding author: Joachim Wassermann (j.wassermann@lmu.de)

Department of Earth and Environmental Sciences, LMU Munich, Theresienstrasse 41; 80333 Munich, Germany

Keypoints:

- First six-degree-of-freedom measurements with a network of rotational motion sensors at an active volcano
- Identification of three visually different types of explosion quakes at Stromboli
- Localization of volcanic sources using the concepts of six-component polarization analysis
- Synthetics and real data reveal complex wave field in the near field of a volcanic source

Abstract

Volcano seismology, while its value for surveillance of an active volcano is undebatable, is a very demanding field when it comes to station deployment, maintenance, and finally interpreting the measurements. Most valuable in the past was the deployment of arrays of sensors to evaluate the properties of the entire wavefield in order to classify, locate, and estimate the dominant mechanism of the corresponding sources. While very beneficial, an array of seismographs is very hard to maintain in a permanent installation at an active volcano. With the advent of new instrumentation based on fiber optic technology such as Distributed Acoustic Sensing (DAS) with fiber optic cables as well as Fiber-Optic Gyroscopes (FOG) the measurement of deformation and rotation, i.e., the gradient of the wavefield is feasible. The advantage of the FOG instrumentation with respect to DAS lies in the portability and ease of deployment, which is very similar to standard deployments of traditional seismometers. During a field campaign in summer 2018 we were able to install three FOGs together with classical broadband seismometers in close proximity to the active vents of Stromboli volcano (Italy). We show that with this new six-degrees-of-freedom (6DOF) measurement we are able to analyze the wavefield composition, a property normally reserved for array(s) of seismic sensors. As a first result, we can support earlier array-derived findings that a large portion of the wavefield at Stromboli volcano is formed by SV- and SH- type waves. We also present first locations of these signals facilitating the polarization properties of the combined measurement of gyroscopes and seismometers. They emphasize the benefit of recording wavefield gradients. In addition to these array-like results, the 6DOF recordings show a clear separation of at least three distinct groups of volcanic events of which two are already known and one represents a jetting event that appears nearly invisible for classical seismometers. However, rotational motions - or more general - gradients of the wavefield experience severe distortions by local velocity fluctuations and topography significantly complicating the application of 6DOF techniques at active volcanoes.

1 Introduction

Seismology plays a key role in the surveillance of active volcanoes. The origin of volcano seismology reaches back as far as 1911 when Omori published his pioneering work on the seismic signals during the Usu volcanic eruption in 1910 (Omori, 1911). Since then, the basic idea of applying the concept of seismology at active volcanoes is that the recorded seismic signal together with its associated source processes allows a direct insight into the motion of the sub-surface fluids which will enable the observer to estimate the activity status of the volcano. With the availability of portable and later digital seismographs, the number of seismic experiments and permanent surveillance networks at volcanoes strongly increased. During these years an increasing amount of data was collected, showing more and more the variability of seismic signals at active volcanoes (Minakami; 1960, 1974; McNutt, 1996) as well as their apparent complexity in the involved source processes. This was and still is in contrast to the well established double couple model of tectonic earthquakes. The wealth of different signals led to the absurd situation that some scientists were looking for data that explained their most favorable models rather than the contrary. A large part of the puzzle in volcano seismology was and still is to distinguish between path and source effects both contributing significantly to the recorded ground motion. These problems were partly solved with the appearance of field deployable broadband seismometers (Dreier et al. 1994, Wassermann, 1997, Neuberg and Pointer, 2000) and

the application of seismic arrays (Neuberg et al., 1994; Chouet et al., 1997, Saccorotti et al. 1998; Almendros et al., 1999, Métaxian et al., 2002). While the use of broadband seismometers deployed in the near field of the sources gave new insights into the corresponding mechanisms of volcanic sources (e.g., Chouet et al. 2010; Kawakatsu and Yamamoto, 2007; Lokmer et al. 2007; Ohminato et al., 1998; Jolly et al., 2017), the use of arrays or even better array of arrays allowed a better location of continuous signals, i.e., volcanic tremor (e.g., Eibl et al., 2017; Di Lieto et al., 2007). In addition to the improved estimate of the source location, also the almost always unknown velocity structure and the composition of the wavefield can be analyzed when an array of sensors is used (Almendros et al., 2002; Wassermann and Ohrnberger, 2001). However, these advantages of broadband sensors and seismic arrays come also with a price. The installation procedure of broadband sensors and arrays is much more complicated as for a classical sparse network of short period seismic stations. While broadband seismometer recordings additionally suffer from noise by meteorological effects and dynamic tilt from volcanic activity, the maintenance of a permanently installed seismic array or even an array of arrays proved to be almost impossible. As a consequence, most of the permanent surveillance networks at volcanoes consist of a few broadband stations only. While this seems to be sufficient for the monitoring of “normal” activity, such sparse networks may not detect changes in the volcanic systems or even be able to locate the sources and the source mechanism with the required precision (De Barros et al., 2011).

Since a few years ago new types of instrumentation give hope to overcome at least some of the just mentioned difficulties. While fiber optical cables used in Distributed Acoustic Sensing (DAS) applications promise to reveal up-to-now unequaled dense snapshots of the wavefield and strain recordings, its deployment is still a challenge and the recording units are expensive and very delicate to handle. This restricts the area of deployment to a few special cases or short recording times. In contrast to this large (channel) number (large N) approach, another concept consists in the measurement of the ground motion and the corresponding wavefield gradient with a very high precision at only a few sites. The latter concept of sparse but precise ground motion measurements seems to fit quite naturally to the situation often met at volcanoes, on extraterrestrial planets (e.g., Sollberger et al., 2020). Or the ocean sea bottom (e.g. Lindner et al., 2016). Combining three axes of translational motion (seismometer) with three axes of rotation (e.g., through Fiber-Optical Gyroscopes; FOG) was already shown to be useful in many applications (e.g., Hadziioannou et al.; 2012; Bernauer et al., 2014; Lindner et al., 2016; Donner et al., 2018; Keil et al. 2020; Sollberger et al., 2020). However, most of the advantages could only be shown theoretically or applied to teleseismic signals recorded by expensive and large ring lasers (e.g., Schreiber et al. 2006, Igel et al., 2007; Yuan et al. 2021). While FOGs are known for decades in navigation, a class of highly sensitive devices especially designed for seismology were only recently made available (Bernauer et al., 2012, 2018, 2021; Yuan et al., 2020).

As a proof of concept, we planned and conducted a field experiment at Stromboli volcano (Italy; figure 1) using three broad band seismic stations (Nanometrics Trillium Compact 120 VS and RefTek RT130) in combination with three blueSeis-3A FOGs (www.blueseis.com, 2021). Stromboli volcano was chosen because of its persistent activity, easiness of logistics and mostly stable weather conditions.



Figure 1: a) Map of Stromboli Island (Italy) with the location of the summit network operated by the university of Florence (squares: tilt meter; triangles: broadband seismometers) and the sites of the 6C measurements (pentagons). The site LISC was deployed using the instruments from CROC for a time range of two days. The active vents are indicated by grey circles (SW & NE). b) The photograph gives an impression of the installation procedure. The seismometer and the FOG are placed on the same plate to guarantee identical motion. For a better insulation (seismometer) and to protect the instruments from wind the pit was refilled with volcanic ash.

2 Experimental Design and Data

Stromboli volcano (Italy) is well known for its persistent activity reaching back more

Journal Pre-proof

than 2000 years which baptized a whole eruption style as “strombolian activity” (Newhall and

Journal Pre-proof

Self, 1982). Next to the continuous tremor which fluctuates in amplitude depending on the

Journal Pre-proof

surface activity, the “normal” behavior of Stromboli volcano consists of frequent small-scale

Journal Pre-proof

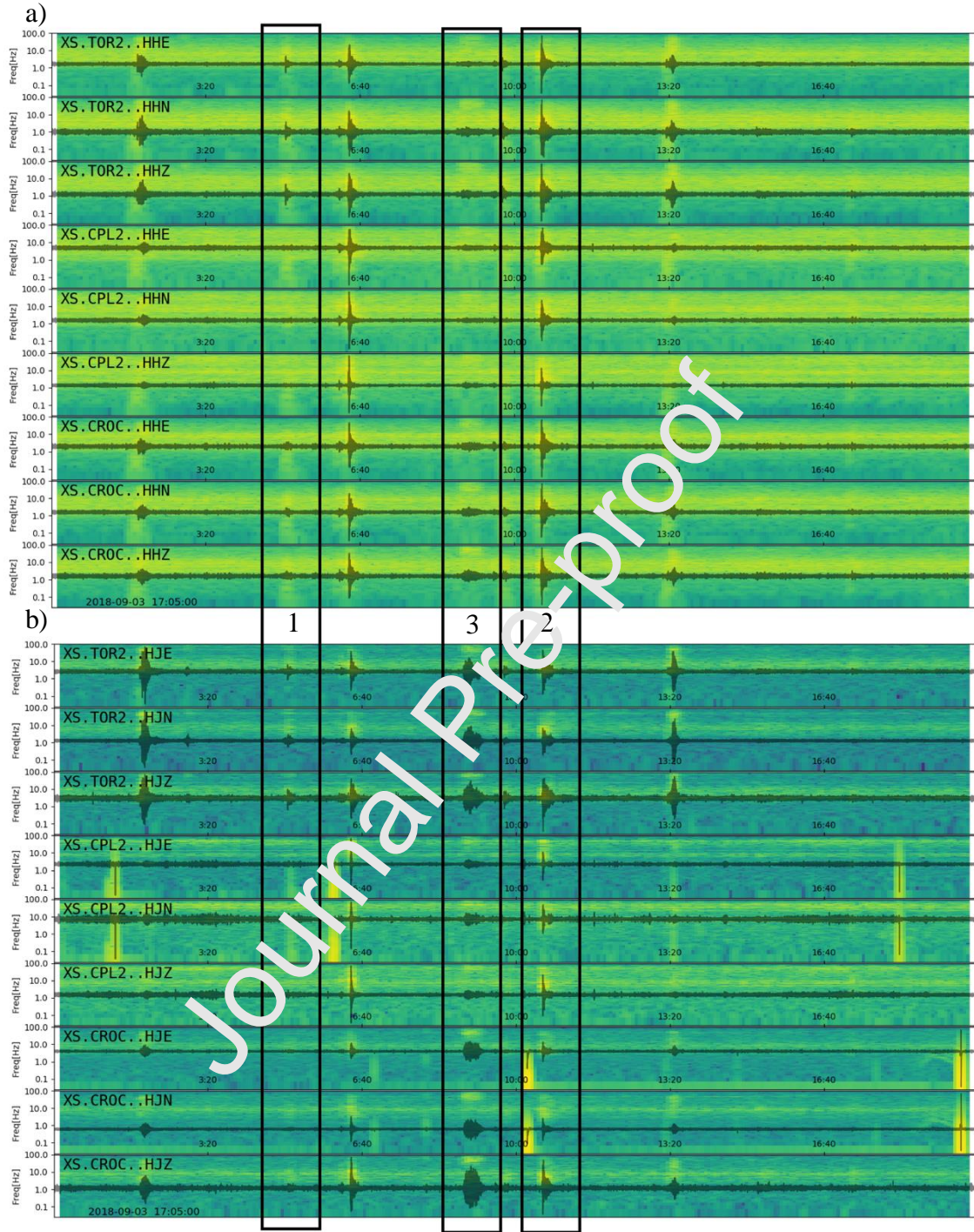


Figure 2: 20 min of data of the network (Fig. 1) recorded with translational seismometers shown in a) and the corresponding rotational motion data b). Both plots are trace normalized and the corresponding spectrogram between 0 -100 Hz is shown as background with lighter colors for larger amplitudes. In order to be directly comparable, the seismometer data are differentiated to be proportional to m/s^2 . The black boxes indicate three apparently different types of volcanic signals with different surface activity to follow.

eruptions, which are associated with the bursting of large gas slugs or churns at the free surface

of the open vent system (e.g., Braun and Ripepe, 1993; Ripepe et al., 1996; Ripepe et al., 2001).

In the last three decades numerous seismic experiments were conducted at Stromboli. Noteworthy of which are e.g., Dreier et al. (1994), Neuberg et al. (1994) and Wassermann (1997) installing portable broadband seismometers the first time, Neuberg et al. (1994), Chouet et al., (1997); Saccorotti and Del Pezzo (2000) analyzing data from seismic arrays, Ripepe et al. (2009) running a permanent network of seismometers, tilt meter and acoustic sensors at the summit of Stromboli volcano (see Fig. 1). Most of these studies explain the dominant low frequency part of the seismic signals as being caused by an ascending gas churn (sometimes also referred as slug or plug) which bursts into fragments when reaching the surface of the magma column. The location of the bursting surface and the start of the seismically detectable ascent of these gas churns varies between 200 and 800 m below surface, respectively (Chouet et al, 2003; Marchetti and Ripepe; 2005). Several studies also showed that the surface appearance of the explosions is imprinted on the seismic broadband recordings. A frequent observation is that the seismic recordings can be divided into two fundamental groups, of which one is associated with the classical Strombolian activity while the other might be seen as a more “muffled” source, which is seen as a higher ash laden eruption plume (e.g., Chouet et al. 2003; Kirchdörfer, 1996). The persistent volcanic tremor shows a strong fluctuation in its amplitude which is often related to changes in the surface activity of the volcano (e.g., Langer and Falsaperla, 1995).

Several array applications as well as traditional 3C polarization analysis showed that a large portion of the wavefield of the volcanic tremor as well as the Strombolian explosion signals consists of SV- and SH-type waves, which demand an explanation of the associated source effects (Chouet et al, 1997; Wassermann, 1997). Prudencio et al. (2015) also showed that a large part of the observed wavefield complexity is caused by strong scattering, while Wielandt and Forbriger (1999) demonstrated that the broadband recordings contain a significant portion of near-field dynamic tilt effects. The wealth of collected multi-disciplinary observations and knowledge about the volcanic activity, the associated seismic signals and the internal structure in addition to the relative ease of accessibility makes Stromboli volcano a top destination for testing new equipment and surveillance techniques.

During the experiment between end of August and mid of September 2018, the activity of Stromboli volcano was rather mild with a few Strombolian eruptions per hour originating from the NE crater (see Fig. 1) and, less frequent, ash-laden explosions from the SW crater. In addition to this quite common behavior, a very pronounced jet activity accompanied by very loud audible sound but barely visible products was completing the spectrum of volcanic surface activity. The mildness of activity enabled and also constrained an installation of the sensors close to the volcanic centers. Figure 1 gives an overview of the station setting with respect to the activity centers. The installation of the occupied sites consisted each of a Nanometrics Trillium Compact 120 SV seismometer, which was installed on the same base plate as the co-located iXblue blueSeis-3A rotational motion sensor (Fig. 1b). For a better insulation of the seismometer and sufficient protection of the sensors from wind and other environmental influences the sensors were installed in a shallow pit and covered by volcanic ash after the deployment. Both sensors were sampled with a rate of 200 Hz and a GNSS driven time synchronization. The still high-power consumption of the blueSeis-3A demanded the installation of a battery with a capacity of 65 Ah as well as a 140 Watt solar-cell at each site. However, even with this quite oversized power source it was not possible to guarantee a continuous 24/7 recording as either the weather or the site conditions (sparse sun light on the panels because of the location of the

sensor) did not allow the complete re-charge of the attached batteries during day light. An additional flaw of the data was caused mainly by the third deployed blueSeis-3A sensor installed at the site CROC (and LISC; Fig. 1a)). This sensor was still in a prototype stage and appeared to produce a large number of spikes, which made most of the recorded data not usable at the end.

The standard treatment of the seismometer data consisted in the conversion of the RefTek (RT130) native format into miniSEED using the ObsPy software library (Beyreuther et al., 2010; Megies et al., 2011). The blueSeis-3A data, which are already digital and in miniSEED format, were “de-ramped” before final storage. The “de-ramping” mechanism is needed in order to clean the data from spikes introduced by the closed-loop operation of the FOG (Guattari et al., 2019).

Figure 2 gives a 20 min example of the final raw 6C recordings at all three simultaneous running sites (Fig. 1). For a better overview of the overall signal properties the background of the trace normalized amplitude-time plot is the corresponding spectrogram of each individual trace. In order to directly compare the recordings of translational to rotational ground motion, the translational, seismometer data are differentiated to be proportional to ground acceleration (e.g., Sollberger et al., 2020). The most obvious feature visible in figure 2 is the existence of different seismic signal types, a finding, which was often made in the past (back boxes in figure 2; e.g., Wassermann, 1997). While type 2 shows the clearest signal in acceleration and rotational motion with an emphasis to higher frequencies, type 1 shows only small to moderate amplitudes in the frequency range above 1 Hz but an enhanced excitation of lower frequencies. This finding is in line with those of Wassermann (1997) and Chouet et al., (2003), who identified apparently similar types during an also mild activity period of Stromboli volcano in 1994 and 1997, respectively.

A completely different class of signals can be seen in figure 2 marked as type 3, which was also reported by Goto et al. (2014). While this signal is hardly visible on translational ground velocity motion recordings it shows up with larger amplitudes on recordings proportional to acceleration and large amplitudes on the rotational motion sensors, respectively. Visual observations at the summit link this type of signals to the occurrence of strong gas jetting events. During this jetting very loud audible noise (comparable to a turbine engine) was produced without any preparation phase or any visual products like rocks or lava fragments expelled from the vent. In a later stage the surface location of the jetting could be identified as a newly developing vent, which by the time of being visible produced sporadic fragments of expelled magma by simultaneously significant reduced sound. Another surprising feature of these jetting events is that they seem not to produce any infra-sound signals on the summit infra-sound stations (0.01 – 10 Hz). Assuming simple plane-wave propagation as a first proxy and considering the proportionality between acceleration and rotation rate, this amplitude difference is in line with a very low propagation speed of the corresponding waves. A plausible explanation for these type 3 events is that the recordings represent acoustic or seismo-acoustic waves coupling into the ground (e.g., Braun and Ripepe, 1993).

3 Analysis

As the mild activity produces rather small amplitudes, we follow the approach of Dreier et al. (1994) and - in a first step - try to identify members of similar waveform groups (i.e., type 1 & type 2) and then increase the signal to noise ratio at least in the lower frequency range by stacking the corresponding group members. A visual inspection of type 3 events (jetting)

revealed a strong variation in duration of the individual events so we exclude this type for the moment from the following analysis steps.

Cluster Analysis

In order to evaluate the questions about the existence and number of clusters of different explosion quakes (i.e., Strombolian eruptions) in more detail, we first run a detection algorithm across the continuous data stream to separate explosions from background tremor.

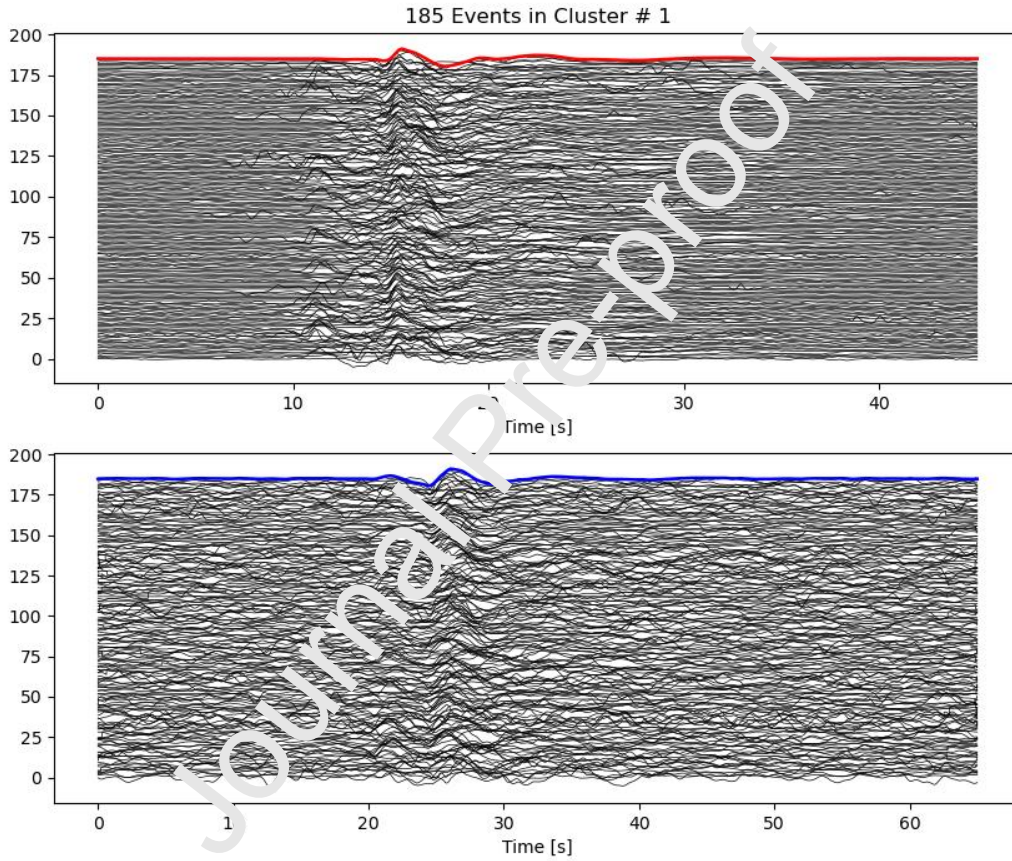


Figure 3 a): Stacking the waveforms of all type 1 events using the Up/Down (Z)-component of translational motion (upper panel a)) and North/South (N)-component of rotational motion (lower panel a)) of station TOR2 in the frequency band 0.1 - 1 Hz. The stacked result is indicated by the uppermost red and blue line, respectively. The number of cluster members is given on top of the figure

The easiest way to perform detections is to apply a (multi-channel) trigger followed by a coincidence estimate. Here, we keep the detection algorithm as simple as possible and apply a standard recursive STA/LTA trigger algorithm followed by a coincidence sum estimation both implemented in ObsPy (Megies et al., 2011). In the following a three channel (vertical component) coincidence on data of all parallel seismometer deployments (TOR2, CPL2, CROC;

s. figure 1) was used together with a coincidence sum of at least two, i.e., the explosion needs to be seen on at least two stations (see Appendix C for detailed settings). The application of the detection results in more than 1400 individual positive triggers during the approx. 10 days of recording. A visual inspection of the trigger performance revealed a high number of false triggers, which was accepted as the next analysis step will filter out most of these false triggers.

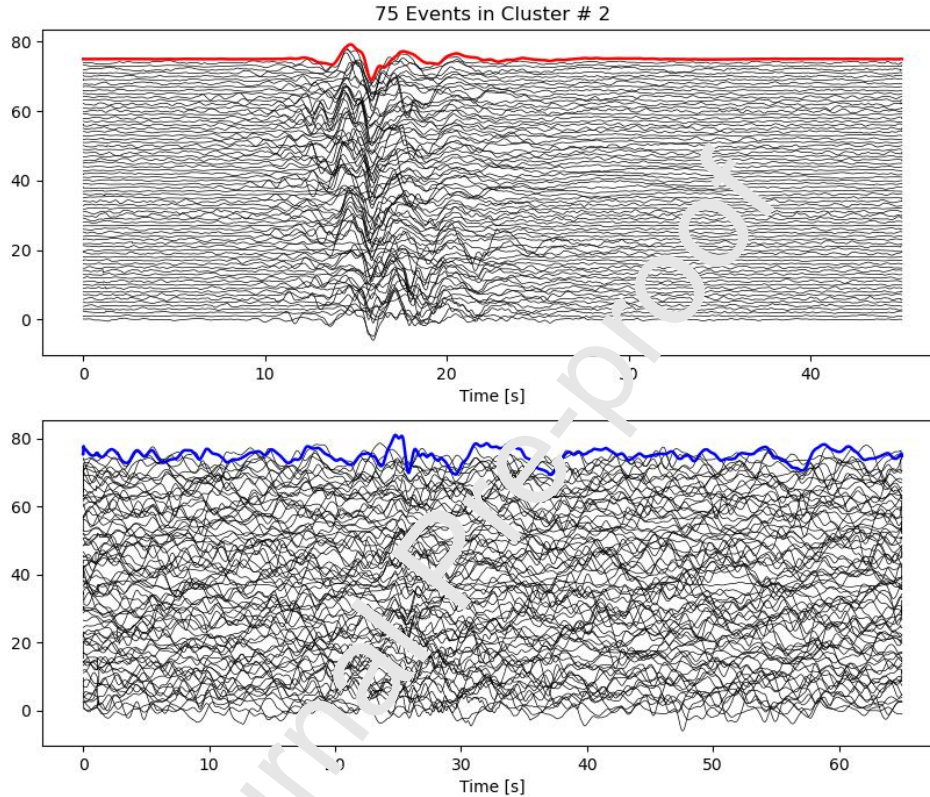


Figure 3b): Stacking the waveforms of all type 2 events using the Up/Down (Z) - component of translational motion (upper panel a)) and North/South (N)-component of rotational motion (lower panel b)) of station TOR2 in the frequency band 0.1-1 Hz. The stack result is indicated by the uppermost red and blue line, respectively. The number of cluster members is given on top of the figure.

This step consists of cross-correlating the individual triggered seismograms and the following cluster determination .

The waveform features to be further analyzed consist of the corresponding cross-correlation functions, which were computed for each combination of waveforms from the Z-component (vertical) channel of station TOR2. While the station TOR2 was chosen because of its overall best signal-to-noise ratio, the Z-component of the seismometer appears to be the “cleanest” record without any additional signals involved (e.g., tilting of horizontal components; spurious spikes on the rotational components). The corresponding time interval was estimated by the trigger onset time including a pre-trigger buffer. All traces were cut to the same length (80 s) and

TOR: Type 1

TOR: Type 2

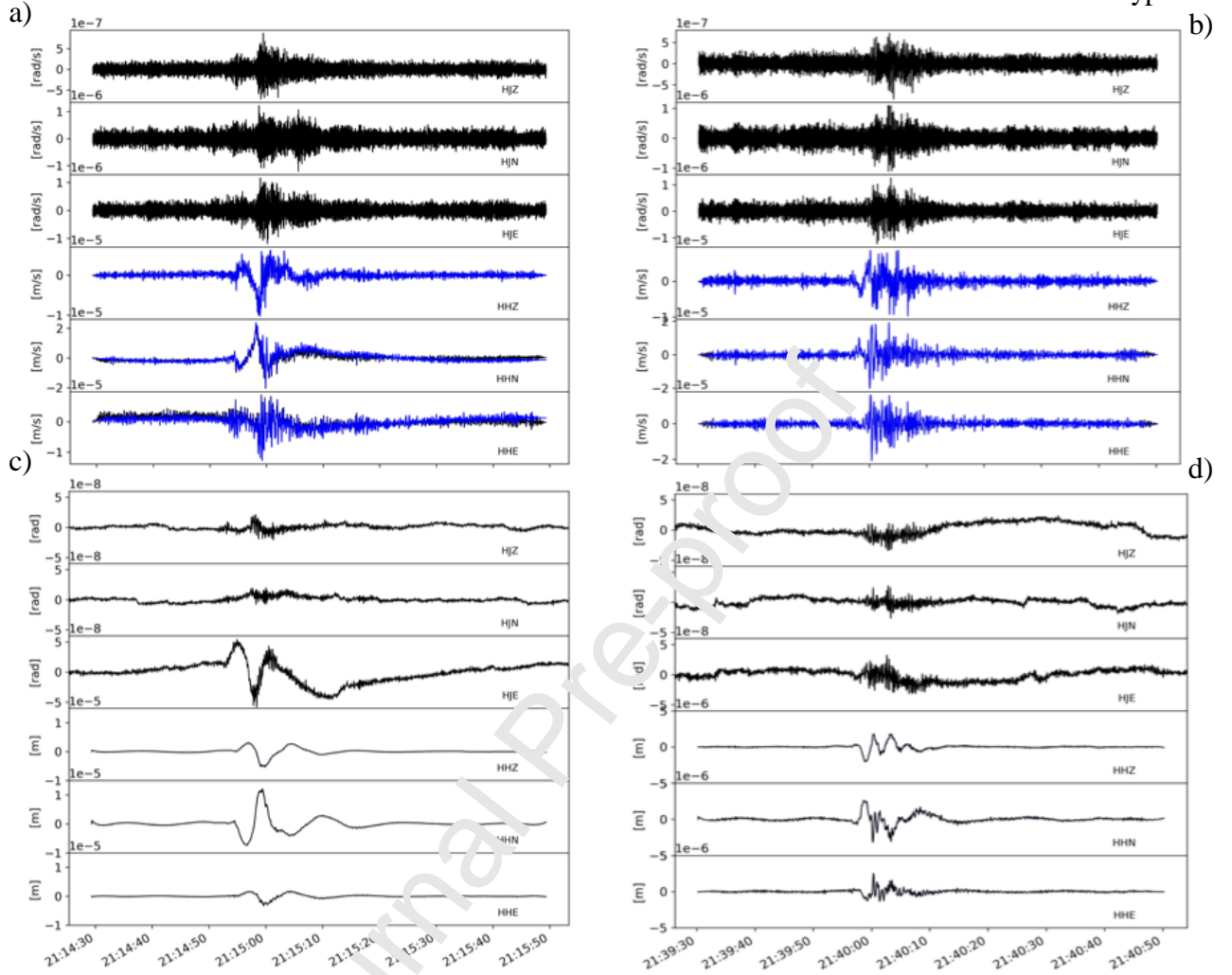


Figure 4: Unfiltered stacked waveforms of type 1 (a) and type 2 (b) explosion quakes at station TOR2. The first three traces corresponds to the rotation rate and the fourth to six traces in blue to the tilt-corrected translational motions, respectively. Underlying the blue traces are the original stack result of the horizontal translational components, which are only visible at type 1 a). In c) and d) the traces are integrated to be proportional to ground displacement and rotation angle, respectively.

pre-filtered in the frequency band between 0.1 - 1 Hz to enhance the correlation result. In addition to the maximum correlation coefficient and its associated dissimilarity coefficient (i.e., $1 - \text{maximum correlation}$) also the shift needed to achieve this correlation was memorized.

To discriminate different clusters the python based DBSCAN algorithm (Schubert et al., 2017, Pedregosa et al., 2011) was applied to the calculated dissimilarity matrix. DBSCAN was chosen as a priori knowledge on the number of possible clusters is not needed and because of its rather simple parameter setup (only two parameters are to be selected; Schubert et al., 2017). The core data model of DBSCAN uses a minimum density level estimation and is based on a threshold of

numbers of neighbors, which are within a search radius with an arbitrary distance measure (Schubert et al., 2017). Only two parameters have to be selected: the radius (and its measure) and the minimum numbers of neighbors to nucleate a cluster. Applying the DBSCAN algorithm to the dissimilarity matrix with an Euclidean distance radius of 0.15 and a minimum samples number of four resulted in two distinct and populated clusters. It has to be kept in mind that the search radius is not directly mapped into similarity or dissimilarity as also bridging samples are allowed (i.e., density connected points). As additional constrain and to better control the stacking process only those traces were used for which the cross correlation exceed the value of 0.7. Figure 3 shows the individual cluster members and the final stack for the corresponding clusters

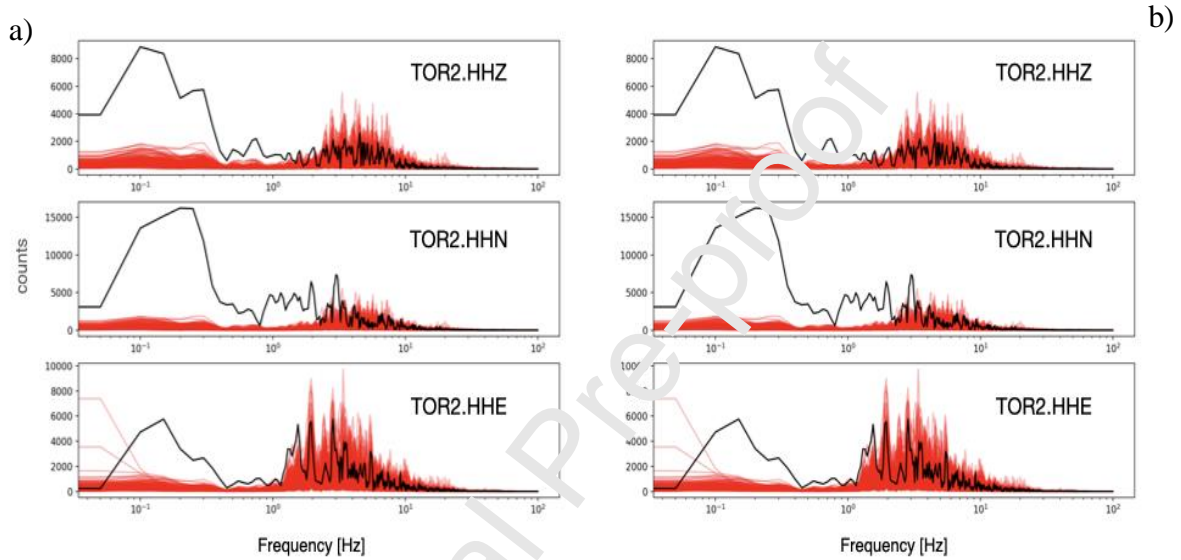


Figure 5: Amplitude spectra of the individual cluster members in red and the amplitude spectra of resulting stack in black are shown in their three components. In a) the corresponding spectra of type 1 and in b) the spectra of type 2 are shown, respectively. All shown spectra are proportional to ground velocity recordings of translational seismometers.

of type 1 and 2 for the filtered (0.1 – 1. Hz) vertical component of seismic station TOR2 (red) and the corresponding rotational component of the N-axis (blue). In the case of the rotational motion recordings the stacking only will successfully increase the signal-to-noise ratio of the desired signal, if the individual signals to be stacked are exceeding the instruments self-noise level, which is around 10-30 nrad/s in the frequency band between 0.1- 4 Hz (Bernauer et al., 2018).

Stacking the data was finally performed using the timing of the estimated cluster members for all available stations and channels without pre-filtering. Stacking of the traces intrinsically assumes that the source location as well as the source mechanisms are- within certain bounds - equal. As the cluster discrimination was based on cross correlation of band-pass filtered traces, we cannot expect that the source area and the source mechanism is better resolved as within the chosen tight frequency-wavelength bounds. By stacking the unfiltered traces, however, we perform a “data-driven” low-pass filtering, which might result in a better resolution of the wavefield properties at least in the best case. Figure 4 gives the 6DOF recordings of the

corresponding stacks of type 1 and type 2 for station TOR2. The improved signal-to-noise ratio of the stacks (Fig. 4) now makes a detailed analysis of the corresponding signals more feasible. Especially in the frequency range between 0.1 to 4 Hz an enhancement of the signal to noise ratio is visible (Fig. 5). While until this point not much new information is gained by the use of 6C recordings, the polarization properties of 6DOF (Sollberger et al., 2018; 2020) recordings makes it now possible to strip down the seismograms to their individual wave field components.

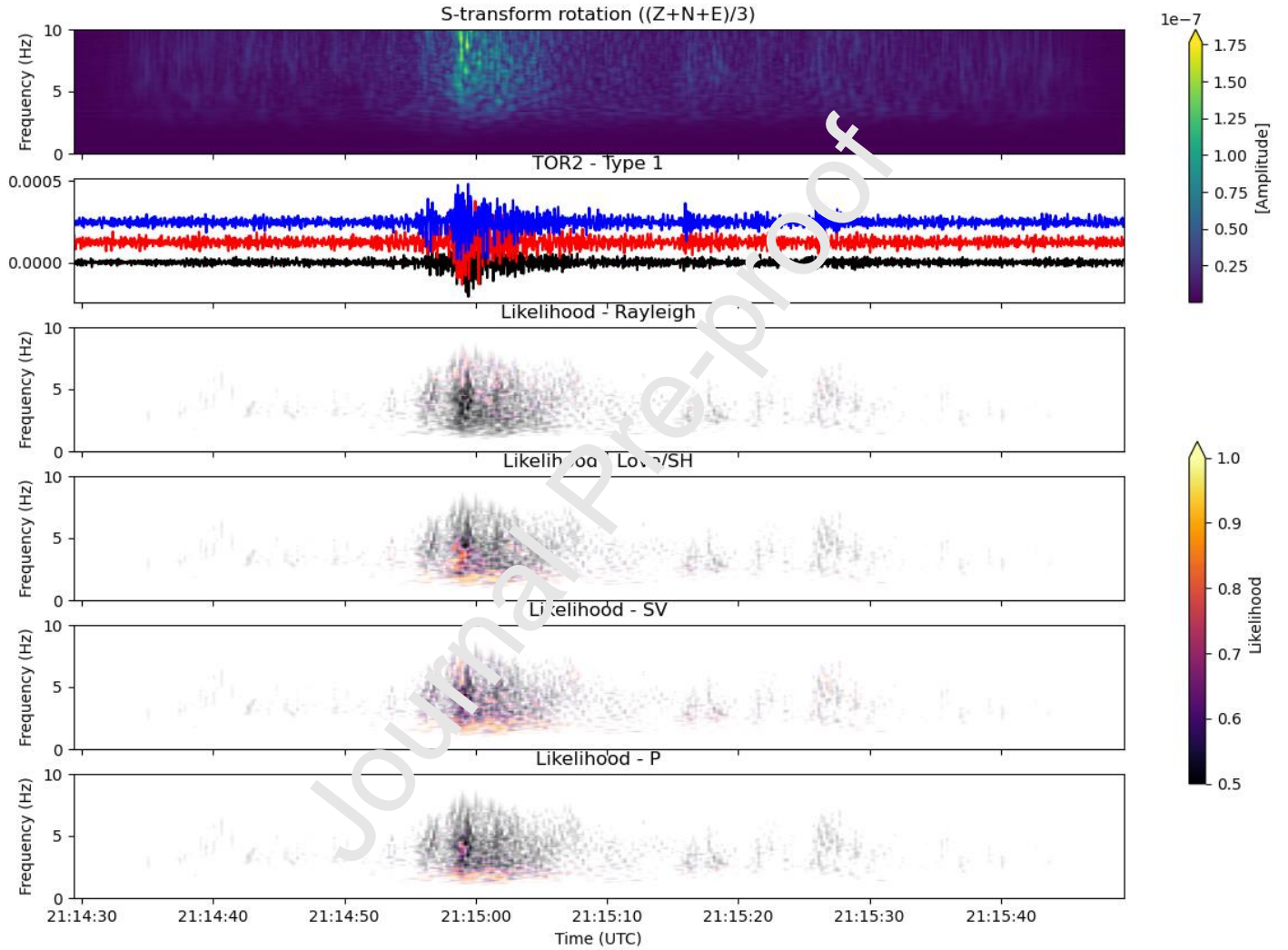


Figure 6: Likelihood maps resulting from the 6DOF polarization routine after Sollberger et al. (2020). The spectrogram (Stockwell (S-)transform; Stockwell et al., 1996) corresponds to the component wide averaged amplitudes of the rotational recordings. The colored traces below represent the up/down, north/south and east/west translational accelerograms of the stacked type 1 events. In order to highlight those portions of the signal where the rotational signal has the highest signal-to-noise ratio, the opaqueness of likelihood maps is driven by the averaged spectrogram. The highest likelihoods (warmer colors) are visible for the SV and SH/Love wave polarization models. While Rayleigh wave models appear to be rather unlikely, the P-wave model shows a higher likelihood in the frequency band between 0.1 - 4 Hz as well.

6DOF analysis

Several authors have claimed that using 6DOF polarization analysis makes it possible to gain similar information about the content of a wavefield as by using an array of seismic translational motion sensors. Most of these claims were either based on theoretical considerations (Donner et al., 2017; Sollberger et al., 2018) or restricted to back azimuth estimations of Love waves and the corresponding apparent phase velocities using high quality ring laser data (e.g., Igel et al. 2005, 2007, 2012; Yuan et al., 2021).

Up to now only few measurements were performed directly at or near earthquake ruptures or volcanic sources (e.g., Wassermann et al., 2020). A first step into the direction of a full 6DOF polarization analysis was done recently by Sollberger et al. (2020) again using high quality ring laser rotational signals. In principal, the 6DOF analysis by Sollberger et al. (2020) is estimating the wavefield properties by additional constraints on the polarization properties of the different wave-types in the rotational motion signal. In a grid based or global search a 6DOF polarization model vector, consisting of P- and S-wave velocity, incidence angles, back azimuth a possibly ellipticity, is tested against the data (mainly amplitude ratios and amplitudes on different components). This test results in a likelihood or residuum of the inverted ratio of the noise-subspace as similarity measure.

We apply exactly the same procedure as described in Sollberger et al. (2020) to analyze the estimated stacked and differentiated translational seismograms (i.e., accelerograms) as well as rotational motion rates. Inherently, we assume that the stacked traces preserve their overall behavior though possibly higher frequencies are suppressed. As a further step we also apply a dynamic tilt correction to the signals of type 1 as they appear to show tilts on the horizontal components in the lower frequency range. In so doing, we apply a modified version of the technique described by Bernauer et al. (2020) using directly the rotational signals as input for the correction.

By applying the 6DOF polarization analysis to the results of the clustering and stacking several assumptions are made. Beside the assumed common source location and source mechanism during stacking, the application of the method by Sollberger et al. (2020) additionally is strictly only valid for plane wave propagation in the far field of the source. A further restriction is the under-critical incidence of SV-waves to the free surface. While in principle possible in theory, the application of 6DOF polarization analysis is further restricted by presence of noise in the signal, which make the estimates of the corresponding phase velocities as well as the incidence angle quite unreliable. As we want to demonstrate what is possible even with a sparse monitoring network, we first ignore these restrictions and will revisit them later.

The application of the 6DOF analysis revealed some surprising details about the wave field composition during the explosion quakes (Fig. 6 & 7). While the complete set of 6DOF analysis results (TOR2: type 1, type 2; CPL2: type 1, type 2) are shown in the appendix A, we will focus here on the station TOR2 and type 1 event as this combination shows the overall best signal-to-noise ratio. The likelihood estimates, i.e., the measure how good does a particular polarization model fit the data, shows a preference to SV/SH-type motions at least in the frequency range between 0.1 – 4 Hz (Fig. 6). For higher frequencies the averaging property of the waveform stacking as well as the increasing influence of other signal sources (e.g., acoustic signals) the 6DOF estimates appear not to be too reliable, but a trend towards Rayleigh-type

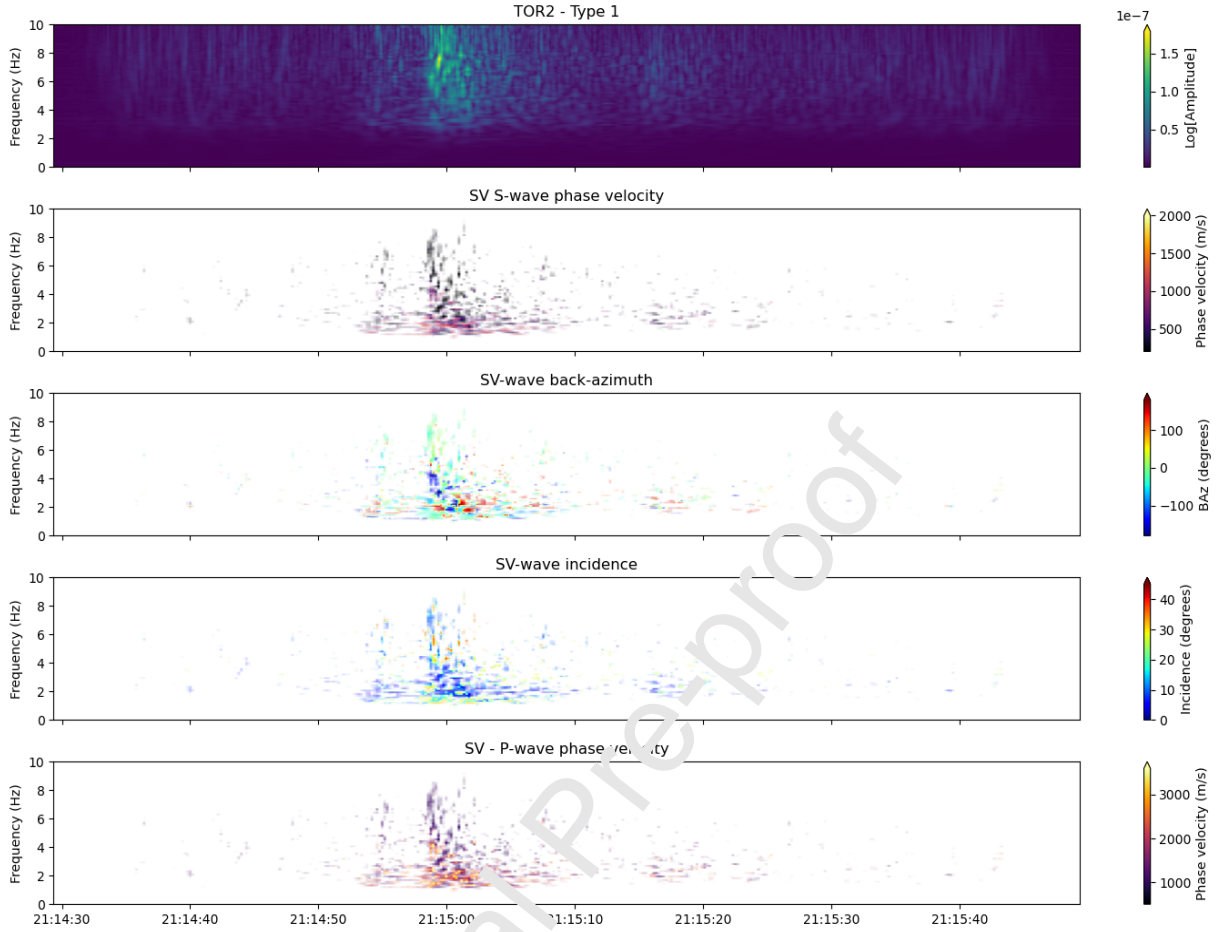


Figure 7: Detailed results of the 6DOF polarization analysis applied to the stacked traces of type 1 event at station TOR2 and the SV-wave model. The corresponding likelihood times the normalized averaged spectral amplitude map of the rotational motion components are used as opaqueness to emphasize the time-frequency bins where the model fits the data best and sufficient wave energy is recorded. For better visibility the opaqueness is clipped at values higher than 0.7. The BAZ and the incidence are measured from north and vertical, respectively.

waves has to be mentioned. While it is impossible to distinguish between Love and SH-waves without further assumptions (i.e., velocity model), it is clear that the wavefield during an explosion is dominated by SV-type motions rather than Rayleigh waves. Noting the close distance to the source region, the analyzed frequency band and the range of wave speed, the lack of surface waves regardless of its type can be easily explained. At this point, we also want to clarify the terminus “explosion quake”, in contrast to regular (chemical) explosions, volcanic explosions are modeled as a combination of tensile faulting and isotropic motion (e.g., Chouet et al., 2003), which generates a significant amount of S-waves also visible in this study.

The 6DOF analysis also makes it possible to estimate the back azimuth (BAZ) and velocity of the corresponding wave package as well as the incidence angle at least in case of SV-waves. Figure 7 gives the corresponding estimates for the SV-wave model. The BAZ shows a large variation around the directions towards the craters with a tendency to point towards north-

west (blueish colors). The incidence angle indicates a very deep source and/or a steep traveling SV-wave. This, however, is in contrast to the incidence-angle estimates of the P- and SH- wave models not shown here but indicating a much larger, possible overcritical incidence (see appendix A). The most likely explanation for this obvious discrepancy is a violation of the assumptions inherently made in the 6DOF polarization analysis. Sollberger et al. (2018, 2020) restrict the valid incidence angle of SV-waves to under critical incidence, which is in case of Stromboli as low as 30° from vertical.

In order to evaluate the capabilities of 6DOF measurements to locate the origin of the seismic waves produced during explosions with somewhat reduced number of assumptions, we next choose a more statistical based approach to evaluate the wave field rather than applying a detailed wave type model on already averaged (stacked) signals.

ROCHADE (Rotational multi CHannel Arrival Direction Estimation)

Because of its computational costs the 6DOF polarization analysis in its present form is only applicable to a few selected events rather than to a continuous data set. In order to estimate the main direction of different types of the volcanic explosion signals and the background signal known as volcanic tremor, we apply a technique developed for the analysis of ambient noise in the framework of microzonation or continuous seismic signals (ROLODE/ROCHADE; Wassermann et al., 2016; Wassermann et al., 2020; Reil et al., 2020; Yuan et al., 2021). In this case neither the velocity nor the incidence angle are accounted for, which are also the most unreliable estimates when the (rotational) signal amplitudes are low, but only the direction estimate is used for further interpretation. The basics of the ROCHADE algorithm consist in a rather simple orthogonal distance regression (ODR) approach in case of horizontal rotational motions (SV-type waves), and a combined search for best fitting rotation of the horizontal translational accelerograms and a successive ORD validation of the fit between transverse acceleration and vertical rotation rate in case of probing for SH-type waves (Wassermann et al., 2016; 2020). For a flat, layered earth the azimuth estimation should be unbiased even if close to the source. In doing so, either the horizontal components of the rotation rate are used, which contains the SV/Rayleigh type waves, or the vertical rotation rate and the horizontal components of the seismometer are chosen, which are sensitive to SH/Love-waves, respectively. While the BAZ estimate of SH-waves needs the angle of rotation to be iteratively (or by a brute force grid search) inverted from the transverse acceleration and vertical rotation rate, SV-type waves can simply be tracked by using the horizontal components of the rotational motion sensors. The 180° ambiguity commonly present in polarization analysis, without further assumptions of the source, can be resolved in the simplest case of SV-type waves by comparing the resulting transverse rotation rate to the vertical acceleration recording of the seismometer. If the corresponding traces are in phase one has simply to add 180° to estimate the correct BAZ value (Yuan et al., 2021; Wassermann et al., 2020). For SH-wave motions the 180° ambiguity can be similarly resolved but, in this case, adding the 180° is needed when the vertical rotational motion and the transverse acceleration recordings are anti-correlated.

Figure 8 a) shows the BAZ rose diagrams of type 1 events in case of SV type motions (orange) and SH-waves (red) in the frequency band 0.8 – 4 Hz. This frequency band was chosen as the 6DOF polarization analysis revealed quite high likelihoods and significant energy for

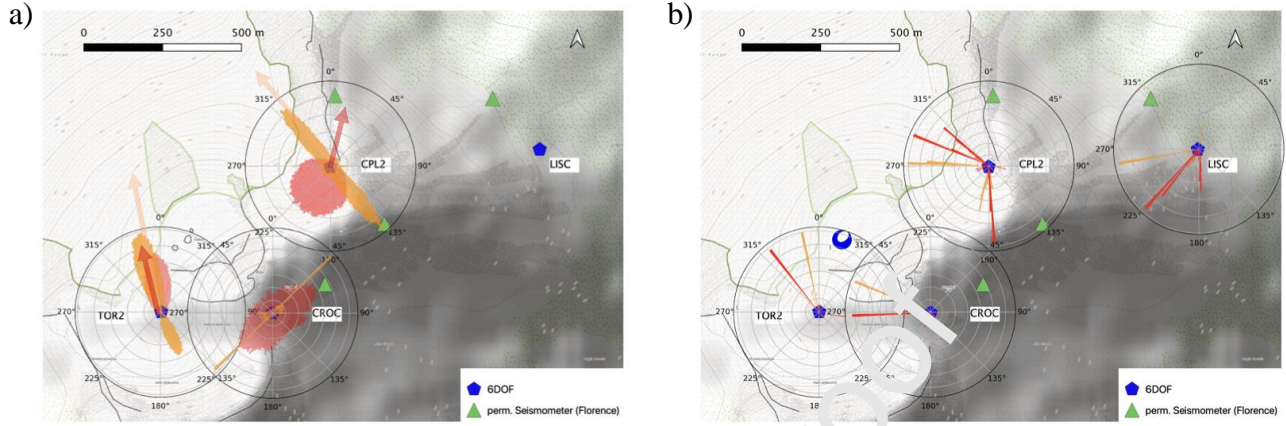


Figure 8: BAZ rose diagrams of SV- (orange) and SH- (red) wave types using the 6DOF measurements and the ROCHADE algorithm. In a) the BAZ findings using the classified type 1 events are shown, while in b) the same algorithm is applied on synthetic data using a tensile point source mechanism located at 200 m a.s.l, shown in a beach ball representation in blue and white colors. For computing the corresponding synthetic seismograms the program package SALVUS (Afanasiev et al., 2019) was used. The red and yellow arrows are the weighted time-frequency average estimates of the Sollberger et al. (2020) approach (Fig. 7 for SV-type waves).

these two wave-models (Fig. 6). Figure 8a) also shows the weighted time-frequency averaged BAZ estimates by applying the 6DOF polarization of Sollberger et al. (2020). Surprisingly at first and regardless which method for BAZ estimation is used, not even at the closest station the estimated BAZ are pointing towards the active crater region but to a region somewhere in the sea. While the BAZ estimation of station CROC might be blurred by the faulty FOG device used at this location, the clear deviation of the estimates at TOR2 and CPL2 station with respect to the crater terrace needs an explanation. A very obvious one is: gradients and thus rotations of the seismic wavefield are very sensitive to local heterogeneities and thus topography. In addition, the orientation and type as well as the location of a seismic source with respect to the free surface will also play an important role. As we estimate the BAZ direction using a sliding window approach applied to the entire event, possible strong reflections favored by the orientation of the radiation pattern might work hand in hand with topography to produce larger and longer lasting wavelets from those directions rather than the direct waves. The comparison between 6DOF polarization analysis and the ROCHADE estimation reveals little differences between the two methods in case of TOR2 station, but some discrepancies in case of station CPL2. In this case the analysis of the weaker SH-wave signal results in a pronounced difference between ROCHADE and the 6DOF polarization analysis, possibly caused by the unreliable incidence estimation of the latter method.

For evaluating how much the source mechanism and the location of the source within the volcano (i.e., corresponding to the rough topography) might influence the BAZ estimates, we used the spectral element-based program package SALVUS (Afanasiev et al., 2019) for

computing synthetics of several different source positions and mechanisms. The details of the model setup are given in the Appendix B. Figure 8 b) gives the BAz estimations using a tensile fault mechanism (shown in blue as beach ball representation) located at the location of the craters but 200 m a.s.l., i.e., 400 – 500 m below the free surface and with fault plane orientation that follow the known orientation of the dike system at Stromboli volcano. As source time function a Ricker wavelet with a central frequency of 1.5 Hz is used. The synthetic data are

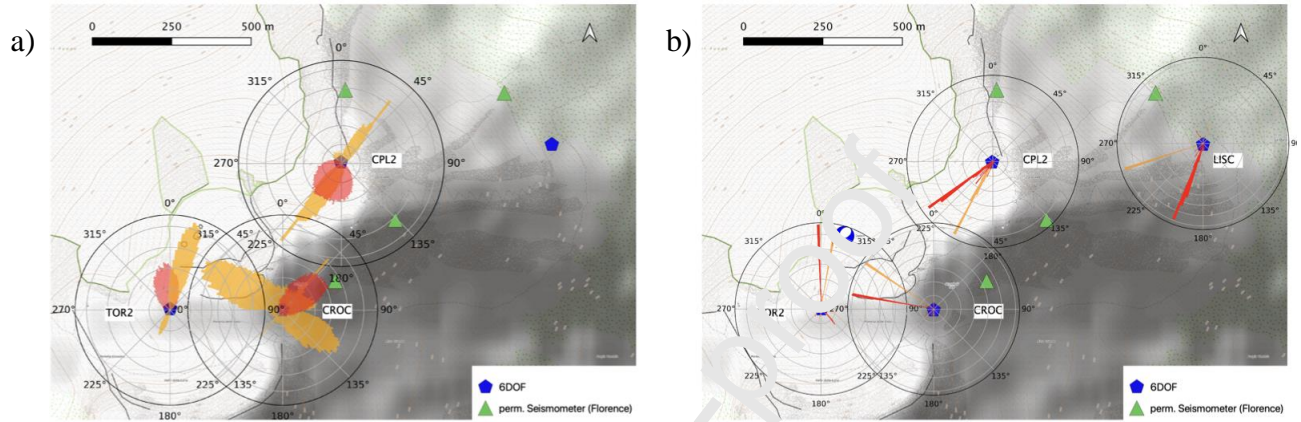


Figure 9: a) Rose diagrams of BAz estimation using SV-waves (orange) and SH-waves (red) of volcanic tremor within the frequency band 0.3 - 4 Hz. The 180° ambiguity at station CROC and CPL2 for the SV-type waves again indicates possible free surface reflections at the topography of the volcano. b) corresponding BAz estimates using synthetic data of a source located at the crater terrace. The agreement of the direction between the real and synthetic SV-type motion estimates indicates in this case a very shallow source location.

treated the same way as the real data (bandpass between 0.8 - 4 Hz) but the energy maximum is obviously centered at 1.5 Hz. Even in this simple example (homogenous velocity model) a significant deviation of the “true” directions at all locations can be recognized.

Figure 9 gives BAz estimates of the different signal models from a four-hour synchronous recording of volcanic tremor at all three 6DOF stations (red - SH-type: transverse acceleration vs. vertical rotation rate; orange - SV-type: radial rotation rate) in the frequency range 0.8 - 4 Hz. This frequency band was chosen to be the same as for the Strombolian eruptions despite the fact that the frequency content of volcanic tremor is much more restricted to the band between 0.8 - 2 Hz. In contrast to the estimates at station TOR2, which point more or less directly towards and is located closest to the active vents, the results at location CROC and CPL2 show a significant portion of the continuous wavefield coming from the opposite direction of the craters. The reason for this 180° ambiguity might be explained again by reflections of the waves at the steep dipping topography surrounding CROC and CPL2.

Another point to be explained is the obvious misalignment of the rose diagram from station CPL2. The SV-type BAz values are pointing slightly more south from the crater terrace. A closer inspection of the estimated directions revealed that the BAz estimates are following the topographic contour lines quite well and thus indicate a very shallow position of the source at

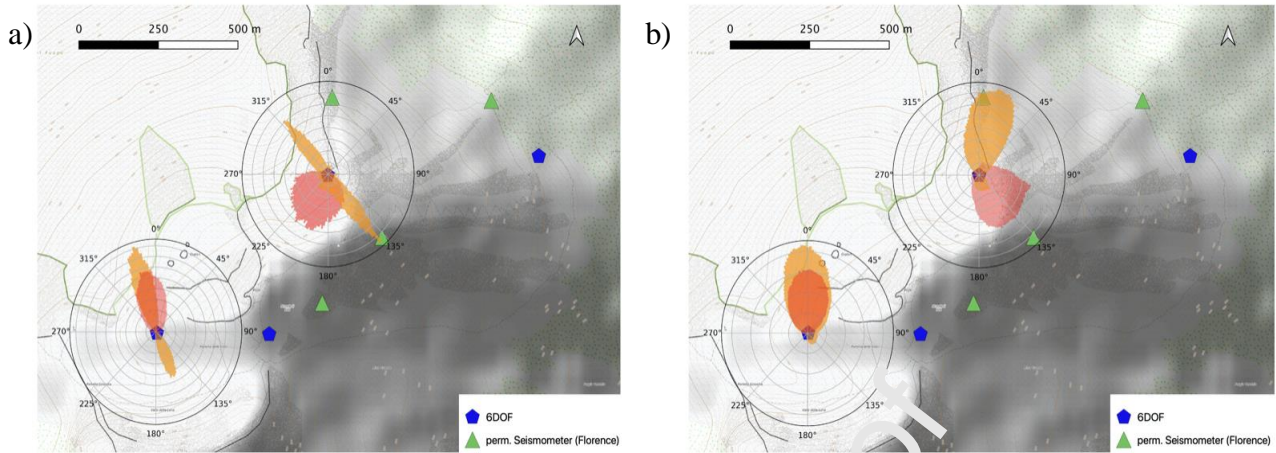


Figure 10: BAz estimates of signal type 3 (see Fig. 2) by the ROCHADE algorithm. While in a) the resulting directions in the frequency band 0.8 - 4 Hz, which represents the starting phase of the signal, indicate a similar source position as in case of type 1 & 2 events, in b) differing directions are estimated in the frequency band 4. - 20 Hz. Direction estimates based on TOR2 data are pointing approx. towards the later visible new vent. BAz estimates at CPL2 are indicating completely different wave paths.

least in the case of the volcanic tremor signal analyzed here. Again, we try to support these findings by computing synthetics. In figure 9 b), the BAz is estimated applying the ROCHADE algorithm on a synthetic data set computed using SALVUS (Afanasyev et al., 2019). In this case the same tensile mechanism shown in figure 8 is located now at 600 m a.s.l and thus only approximately 100 m below the crater terrace. Surprisingly in this case the BAz estimates of synthetics and the real data are matching quite well indicating a very shallow source location of the volcanic tremor centered at the crater terrace (see figure 9 a and b). In the synthetic case the SV-type motion at CPL2 is polarized parallel to the isohypses as well. While the shallow source depth of volcanic tremor was already proven in several other studies, it is important to note when looking on figure 9b) that even at a station further away (LISC) a still significant mis-alignment of the SH-type BAz is visible even in the simulated seismograms.

Finally figure 10 gives the BAz estimates of the type 3 jetting events. For this signal class we divided the ROCHADE analysis into two different frequency bands: 0.8 - 4 Hz (Fig. 10a) and 4 - 20 Hz (Fig. 10b) in order to account for the pronounced higher frequency content of this signal class. While the BAz estimates of type 3 events in the lower frequency band (0.8 - 4 Hz) and thus the start phase of the signals are more or less consistent with the dominant directions found for type 1 and 2 events and thus indicating a similar position of the starting phase of these events, the later appearing, long lasting and higher frequency part of the signal (4 - 20 Hz) indicate a different source position for this part of the wavefield. In fact, TOR2 data points to a region, which coincides with the direction to a later visible newly developing vent. However, the direction finding at station CPL2 indicates a completely different travel path. To explain this deviation, we are revisiting the recordings of the individual events. Assuming for now a plane-wave propagation the amplitudes of translational acceleration scales with the corresponding rotation rate. The scaling factor is then simply a multiple of the apparent wave velocity (e.g., Igel

et al., 2005). A rough calculation of the ratio of the corresponding envelopes of the filtered (4 - 20 Hz) acceleration and rotation rate gives values of speed of sound or below. Evidently the large amplitude, high frequency part of the type 3 signal seems to be caused by air or air – coupled waves rather than pure elastic waves. With this in mind a possible explanation of the estimated direction for CPL2 would be caused by an acoustic reflection at the summit area of Stromboli or the steep cliff located just behind the station. What remains unclear, however, is the mechanism, which transform air waves into the ground as SH-type motion, and is clearly to be seen in figure 10b) focusing on the red rose diagram. A further puzzle to be solved is the absence of a clear signal on the infra-sound sensors, which are deployed close by. A part of the reason for this absence is the transfer function of the deployed sensors, which are not fully capable to record the higher frequency portion of the signals.

4 Concluding Remarks

The first application of a multi-station recording of 6DOF seismic motion at an activate volcano revealed the high potential of the new information provided by the rotational components of motion. The property of rotational devices to act as a wave polarizer, i.e., their sensitivity only for S-wave like signals, is one of the key points in using rotational motion sensors. In case of the wavefield at Stromboli volcano it is clearly visible that large portions of the wavefield are made up by SH- and SV-type motion, respectively. In contrast to this surface waves do not play an important role, at least in the considered frequency band between 0.1 – 4 Hz and the close range of distances to the active sources present in this study. While this finding is not entirely new, similar results were published using seismic array data including a much larger source-receiver distance (Chouet et al., 1997), the substantially simpler installation procedure of a single site to achieve these estimates is a key motivation to apply 6DOF on activate volcanoes. Another key point of the analysis presented here is the identification of different types of seismic events. While it is interesting to recognize that some events seem to be better visible on the rotational motion devices, this can simply be explained by the different frequency content of the signals. Rotational rate motions are proportional to acceleration when assuming simple plane-wave propagation. Thus, differentiating the seismometer recordings (or simply high-pass filtering) will result in a comparable signal-to-noise ratio.

At the same time, it also becomes clear that the high sensitivity to local and structural effects makes a direct interpretation of the combined signals, i.e., rotations and translations at least difficult. Care must be taken as soon as topography or local velocity variations play a more dominant role, which makes the comparison of the findings with adequately computed synthetics inevitable. However, this high sensitivity to local structure can also be used to increase the resolution of structural as well as source mechanism investigations. Combining the technique of estimating local 1D velocity profiles (e.g., Keil et al. 2020) or completely correct for the local effects on the strain tensor (Singh et al., 2020) will lead to a much more precise near station velocity model. Using this together with the increasing computer resources and easier to be handled and accurate solvers (e.g., SALVUS; Afanasiev et al., 2019) a much more reliable and possible more detailed moment tensor inversion seems to be feasible (Bernauer et al., 2012; Donner et al., 2017). Yet, a higher sensitivity of the currently available rotation sensors is still necessary to reach these goals. In order to exploit the full potential of this new information much stronger seismic signals are needed as they were present during the 2018 activity at Stromboli, which, on the other hand made a near source observation possible in the first place.

Acknowledgments

The thoughtful and detailed reviews of two anonymous reviewers and the handling by the paper by the editor D. Roman are highly appreciated. All plots and analysis were made using the ObsPy Python environment (Beyreuther et al., 2010; Megies et al., 2011). The help of Lion Krischer (Mondaic) in setting up SALVUS is very much appreciated. All maps were created using QGIS (QGIS Development Team, 2021) and OpenTopoMap (<http://opentopomap.org>, 2021). We gratefully acknowledge support from the ERC-Advanced Project ROMY (contract No: 339991) and the project PIONEERS (Planetary Instruments based on Optical technologies for an iNnovative European Exploration using Rotational Seismology) funded by the Horizon 2020 research and innovation program of the European Commission.

References

- Afanasiev, M., Boehm, C., van Driel, M., Krischer, L., Rietman, M., May, D.A., Knepley, M.G., and Fichtner, A.; 2019. Modular and flexible spectral-element waveform modelling in two and three dimensions, *Geophys. J. Int.*, **216** (3), 1675 - 1692, <https://doi.org/10.1093/gji/ggy469>
- Almendros, J., Ibanez, J., Alguacil, G., and Del Pezzo, E.; 1999. Array analysis using circular wave-front geometry: an application to locate the nearby seismo-volcanic source, *Geophys. J. Int.*, **136**, 159–170.
- Almendros, J., Chouet, B., Dawson, P., and Huber, C.; 2002. Mapping the sources of the seismic wave field at Kilauea Volcano, Hawaii, using data recorded on multiple seismic antennas, *Bull. Seismol. Soc. Am.*, **92**, 2352–2351.
- Bernauer, F., Wassermann, J., Guattari, F., Frenois, A., Bigeur, A., Gaillot, A., de Toldi, E., Ponceau, D., Schreiber, U. and Igel, H.; 2018. BlueSeis3A: Full Characterization of a 3C Broadband Rotational Seismometer, *Seismol. Res. Lett.* **89**(2A), 620 - 629, doi: 10.1785/0220170143.
- Bernauer, F., Wassermann, J. and Igel, H.; 2012. Rotational sensors - a comparison of different sensor types. *J. Seismol.* **16** (4), 595–602.
- Bernauer, M., Fichtner, A., and Igel, H.; 2014. Reducing non-uniqueness in finite source inversion using rotational ground motions. *J. Geophys. Res.: Solid Earth*, **119**(6), doi:10.1002/2014JB011042.
- Bernauer, F., Garcia, R.F., Murdoch, N., Dehant, V., Sollberger, D., Schmelzbach, C., Stähler, S., Wassermann, J., Igel, H., Cadu, A., Mimoun, D., Ritter, B., Filice, V., Karatekin, Ö., Ferraioli, L., Robertsson, J.O.A., Giardini, D., Lecamp, G., Guattari, F., Bonnefois, J.-J., and Raucourt, S.; 2020. Exploring planets and asteroids with 6DoF sensors: Utopia and realism. *Earth Planets Space*, **72**, 191. <https://doi.org/10.1186/s40623-020-01333-9>.
- Bernauer, F., Wassermann, J., and Igel, H.; 2020. Dynamic Tilt Correction Using Direct Rotational Motion Measurements, *Seismol. Res. Lett.* **91**(5), 2872 - 2880, doi: 10.1785/0220200132.
- Bernauer, F.; Behnen, K.; Wassermann, J.; Egendorf, S.; Igel, H.; Donner, S.; Stämmeler, K.; Hoffmann, M.; Edme, P.; Sollberger, D.; et al.; 2021. Rotation, Strain and Translation

- Sensors Performance Tests with Active Seismic Sources. *Sensors*, 21,264. <https://doi.org/10.3390/s21010264>
- Beyreuther, M., Barsch, R., Krischer, L., Megies, T., Behr, Y., and Wassermann, J.; 2010. ObsPy: A Python Toolbox for Seismology, *Seismol. Res. Lett.*, **81**(3), 530-533, doi:10.1785/gssrl.81.3.530.
- Braun, T. and Ripepe, M.; 1993. Interaction of seismic and airwaves recorded at Stromboli volcano. *Geophys. Res. Lett.*, **20** (1), 65-68.
- Chouet, B., Saccorotti, G., Martini, M., Dawson, P., De Luca, G., Milana, G., and Scarpa, R. ; 1997. Source and path effects in the wavefields of tremor and explosions at Stromboli Volcano, Italy, *J. Geophys. Res.*, **102**, 15129–15150.
- Chouet, B., Dawson, P., Ohminato, T., Martini, M., Saccorotti, G., Giudicepietro, F., De Luca, G., Milana, G., and Scarpa, R.; 2003. Source mechanism of explosions at Stromboli Volcano, Italy, determined from moment-tensor inversions of very-long-period data, *J. Geophys. Res.*, **108**(B1), 2019, doi:10.1029/2002JB001919.
- Chouet, B. A., Dawson, P. B., James, M. R., Lane, S. J., 2010. Seismic source mechanism of degassing bursts at Kilauea Volcano, Hawaii: Results from waveform inversion in the 10–50 s band. *J. Geophys. Res.: Solid Earth* <https://doi.org/10.1029/2009JB006661>
- De Barros, L., Martini, F., Bean, C.J, García Yebra, A., and Ibáñez, J.M.; 2012. Imaging magma storage below Teide volcano (Tenerife) using scattered seismic wavefields, *Geophys. J. Int.*, **191**, 695-706, doi:10.1111/j.1365-246X.2012.05637.x.
- Di Lieto, B. Saccorotti, G., Zuccarello, L., La Rocca, M., and Scarpa, R., 2007. Continuous tracking of volcanic tremor at Mount Etna, Italy, *Geophys. J. Int.*, **169** (2), 699–705, <https://doi.org/10.1111/j.1365-246X.2007.03316.x>
- Donner, S., Lin, C. J., Hadziioannou, C., Gebauer, A., Vernon, F., Agnew, D. C., Igel, H., Schreiber, U. and Wassermann, J., 2017. Comparing direct observation of strain, rotation, and displacement with array estimates at Piñon Flat Observatory, California, *Seismol. Res. Lett.*, **88**, 1107–1116.
- Donner, S., Mustac, K., Megani, B., Tkalčić, H., and Igel, H., 2018. Seismic moment tensors from synthetic rotational and translational ground motion: Green's functions in 1-D versus 3-D. *Geophys. J. Int.*, **223**, 161–179. doi: 10.1093/gji/ggaa305
- Dreier, R., Widmer, R., Schick, R., and Wielandt, E., 1994. Stacking of broadband seismograms at Stromboli. *Acta Vulcanol.* **5**, 165-172.
- Eibl, E. P. S., Bean, C. J., Jónsdóttir, I., Höskuldsson, A., Thordarson, T., Coppola, D., Witt, T., and Walter, T. R., 2017. Multiple coincident eruptive seismic tremor sources during the 2014–2015 eruption at Holuhraun, Iceland, *J. Geophys. Res. Solid Earth*, **122**, 2972–2987, doi:10.1002/2016JB013892.
- Goto, A., Ripepe, M. and G. Lacanna, 2014. Wideband acoustic records of explosive volcanic eruptions at Stromboli: New insights on the explosive process and the acoustic source, *Geophys. Res. Lett.*, 41, doi:10.1002/2014GL060143

- Guattari, F., de Toldi, E., Garcia, R. F., and Mimoun, D., 2019. Fiber optic gyroscope for 6-component planetary seismology. *Proc. Int. Conf. Space Optics — ICSO 2018*; 1118080. <https://doi.org/10.1117/12.2536207>
- Hadziioannou, C., Gaebler, P., Schreiber, U., Wassermann, J., and Igel H., 2012. Examining ambient noise using co-located measurements of rotational and translational motion, *J. Seismol.*, **16**(4), 787-796, doi:10.1007/s10950-012-9288-5.
- Igel, H., Schreiber, U., Flaws, A., Schuberth, B., Velikoseltsev, A. and Cochard, A., 2005. Rotational motions induced by the M8.1 Tokachioki earthquake, September 25, 2003, *Geophys. Res. Lett.* **32**, L08309, doi: 10.1029/2004GL022336.
- Igel, H., Nader, M.-F., Kurrle, D., Ferreira, A.M., Wassermann, J., and Schreiber, K.U., 2011. Observations of Earth's Toroidal Free Oscillations with a Rotation Sensor: The 2011 Magnitude 9.0 Tohoku-Oki Earthquake. *Geophys. Res. Lett.*, doi:10.1029/2011GL049045.
- Igel, H., Cochard, A., Wassermann, J., Flaws, A., Schreiber, U., Velikoseltsev, A., and Pham Dinh, N., 2007. Broad-band observations of earthquake-induced rotational ground motions, *Geophys. J. Int.*, **168** (1), 182–196, doi:10.1111/j.1365-246X.2006.03146.x.
- Jolly, A.D., Lokmer, I., Thun, J., Salichon, J., Fry, B. and Chardot, L., 2017. Insights into fluid transport mechanisms at White Island from analysis of coupled very long-period (VLP), long-period (LP) and high-frequency (HF) earthquakes, *J. Volcanol. Geotherm. Res.*, **343**, 75-94, <https://doi.org/10.1016/j.jvolgeores.2017.06.006>.
- Kawakatsu, H., Yamamoto, M., 2007. Volcano Seismology. *Treatise on Geophys.* **4**, 389-420. Doi 10.1016/B978-044452748-5.00073-0.
- Keil, S., Wassermann, J., and Igel, H., 2020. Single-station seismic microzonation using 6C measurements, *J. Seismol.*, doi:<https://doi.org/10.1007/s10950-020-09944-1>.
- Kirchdörfer, M., 1999. Analysis and quasi static FE modelling of long period impulsive events associated with explosions at Stromboli volcano (Italy), *Ann. Geofis.*, **42**(3), 379 - 390.
- Langer, H., and Falsaperla, S., 1996. Long-term observation of volcanic tremor on Stromboli volcano (Italy): A synopsis. *P. Appl. Geophys.* **147**, 57–82.
- Lindner, F., J. Wassermann, M. Schmidt-Aursch, K.U. Schreiber and H. Igel, 2016. Sea-floor ground rotation observations: potential for improving signal-to-noise ratio on horizontal OBS components, *Seismol. Res. Lett.*, doi: 10.1785/0220160051.
- Lokmer, I., Bean, C.J., Saccorotti, G., and Patanè, D., 2007. Moment-tensor inversion of LP events recorded on Etna in 2004 using constraints obtained from wave simulation tests, *Geophys. Res. Lett.*, **34** (22).
- Marchetti, E., and Ripepe, M., 2005. Stability of the seismic source during effusive and explosive activity at Stromboli Volcano, *Geophys. Res. Lett.*, **32**, L03307, doi:10.1029/2004GL021406.
- McNutt, S. R., 1996. Seismic Monitoring and Eruption Forecasting of Volcanoes: A Review of the State-of-the-Art and Case Histories. In: *Monitoring and Mitigation of Volcano Hazards*. Springer, Berlin, Heidelberg. https://doi.org/10.1007/978-3-642-80087-0_3

- Megies, T., Beyreuther, M., Barsch, R., Krischer, L. and Wassermann, J., 2011. ObsPy-What can it do for data centers and observatories?, *Annals of Geophysics*, **54**(1), 47–58, doi:10.4401/ag-4838.
- Métaxian, J.-P., Lesage, P., and Valette, B., 2002. Locating sources of volcanic tremor and emergent events by seismic triangulation: application to Arenal volcano, Costa Rica, *J. Geophys. Res.*, **107**, 2243).
- Minakami, T., 1960. Fundamental research for predicting volcanic eruptions. *Bull. Earth Res. Inst.* **38**, 497 – 544.
- Minakami, T., 1974. Seismology of volcanoes in Japan. In: *Physical volcanology*, L. Civetta, P. Gasparini, G. Luongo and A. Rapolla (eds), Elsevier Publ. Co., Amsterdam, p. 1–27.
- Neuberg, J., and Pointer, T., 2000. Effects of volcano topography on seismic broad-band waveforms. *Geophys. J. Int.*, **143** (1), 239-248. Please check
- Neuberg, J., Luckett, R., Ripepe, R., and Braun, T., 1994. Highlights from a seismic broadband array on Stromboli. *Geophys. Res. Lett.* **21** (9), 749 – 752.
- Newhall, C. G., and Self, S., 1982. The volcanic explosivity index (VEI) an estimate of explosive magnitude for historical volcanism, *J. Geophys. Res.*, **87**(C2), 1231 –1238, doi:10.1029/JC087iC02p01231.
- Ohminato, T., Chouet, B. A., Dawson, P. B., and Neeb, S., 1998. Waveform inversion of very-long-period impulsive signals associated with magmatic injection beneath Kilauea volcano, Hawaii. *J. Geophys. Res.*, **103**, 23839–23862.
- Omori, F., 1911. The Usu-san eruption and earthquake and elevation phenomena, *Bull. Imp. Earthq. Inv. Com.*, **5**, 1–137.
- Pedregosa, F., Varoquaux, G., Gramfort, A., Michel, V., Thirion, B., Grisel, O., Blondel, M., Prettenhofer, P., Weiss, F., Dubourg, V., Vanderplas, J., Passos, A., Cournapeau, D., Brucher, M., Perrot, M. and Duchesnay, E., 2011. Scikit-learn: Machine Learning in Python, *J. of Machine Learning Research*, **12**, 2825-2830.
- Prudencio, J., Del Pezzo, E., Ibáñez, J. M., Giampiccolo, E., and Patané, D., 2015. Two-dimensional seismic attenuation images of Stromboli Island using active data. *Geophys. Res. Lett.*, **42**, 1717 – 1724. doi: 10.1002/2015GL063293.
- QGIS Development Team, 2021. QGIS Geographic Information System. Open Source Geospatial Foundation Project. <http://qgis.osgeo.or> (last visited 29.Jun.2021)
- Ripepe M., Ciliberto S., and M. Della Schiava, 2001. Time constraints for modelling source dynamics of volcanic explosions at Stromboli. *J. Geophys. Res.* **106**(B5), 8713–8727. <https://doi.org/10.1029/2000JB900374>
- Ripepe, M., Delle Donne, D., Lacanna, G., Marchetti, E., and Ulivieri, G.SZ, 2009. The onset of the 2007 Stromboli effusive eruption recorded by an integrated geophysical network, *J. Volcanol. Geotherm. Res.*, **182**(3-4), 131 - 136, ISSN 0377-0273, <https://doi.org/10.1016/j.jvolgeores.2009.02.011>
- Ripepe, M., Poggi, P., Braun, T., and Gordeev, E., 1996. Infrasonic waves and volcanic tremor at Stromboli. *Geophys. Res. Lett.*, **23** (2), 181-184.

- Saccorotti, G., Chouet, B. A., Martini, M., and Scarpa, R., 1998. Bayesian statistics applied to the location of the source of explosions at Stromboli Volcano, Italy. *Bull. Seismol. Soc. Am.* **88** (5), 1099-1111.
- Saccorotti, G., and Del Pezzo, E., 2000. A probabilistic approach to the inversion of data from a seismic array and its application to volcanic signals. *Geophys. J. Int.*, **143**(1), 249 – 261, <https://doi.org/10.1046/j.1365-246x.2000.00252.x>
- Schreiber, U., G. Stedman, H. Igel, and A. Flaws, 2006. Ring Laser Gyroscopes as Rotation Sensors for Seismic Wave Studies, in: *Earthquake source asymmetry, structural media and rotation effects*, edited by Teisseyre R., Takeo M. and Majewski E., Springer Verlag.
- Schubert, E., Sander, J., Ester, M., Kriegel, H.-P., and Xu, X., 2017. DBSCAN Revisited, Revisited: Why and How You Should (Still) Use DBSCAN. *ACM Trans. Database Syst.* **42**(3), Article 19 (July 2017), 21 pp. <https://doi.org/10.1145/3068335>
- Singh, S., Capdeville, Y., and Igel, H., 2020. Correcting wavefield gradients for the effects of local small-scale heterogeneities. *Geophys. J. Int.*, **221**, 995–1011.
- Sollberger, D., Greenhalgh, S.A., Schmelzbach, C., Van Penterghem, C., Robertsson, J.O.A., 2018. 6-C polarization analysis using point measurements of translational and rotational ground-motion: Theory and applications. *Geophys. J. Int.*, **213**, 77–97.
- Sollberger, D. Igel, H., Schmelzbach, C., Edme, P., van Manen, D.-J., Bernauer, F., Yuan, S., Wassermann, J., Schreiber, U., and Robertsson, J. O.A., 2020. Seismological Processing of Six Degree-of-Freedom Ground-Motion Data, *Sensors* **20** (23), 6904. <https://doi.org/10.3390/s20236904>
- Stockwell, R.G., Mansinha, L. & Lowe, P.P., 1996. Localization of the complex spectrum: the *S* transform, *IEEE Trans. Signal Process.*, **44**(4), 998–1001.
- Wassermann, J., 1997. Locating the sources of volcanic explosions and volcanic tremor at Stromboli Volcano (Italy) using beam-forming on diffraction hyperboloids. *Phys. Earth Planet. Inter.*, **104**, 271–281.
- Wassermann, J., and Ohrnberger, M., 2001. Automatic hypocenter determination of volcano induced seismic transients based on wave field coherence - an application to the 1998 eruption of Mt. Merapi, Indonesia, *J. Volcanol. Geotherm. Res.*, **110**, 57 - 77.
- Wassermann, J., Wietek, A., Hadziioannou, C., and Igel, H., 2016. Toward a Single-Station Approach for Microzonation: Using Vertical Rotation Rate to Estimate Love-Wave Dispersion Curves and Direction Finding. *Bull. Seismol. Soc. Am.*, **106** (3), [doi:10.1785/0120150250](https://doi.org/10.1785/0120150250).
- Wassermann, J., Bernauer, F., Shiro, B., Johanson, I., Guattari, F., and Igel, H., 2020. Six-Axis Ground Motion Measurements of Caldera Collapse at Kīlauea Volcano, Hawai‘i - More Data, More Puzzles? *Geophys. Res. Lett.*, **47** (e2019GL085999), [doi:10.1029/2019GL085999](https://doi.org/10.1029/2019GL085999).
- Wielandt, E., and Forbriger, T., 1999. Near-field seismic displacement and tilt associated with the explosive activity of Stromboli. *Ann. Geophys.* **42** (3). <https://doi.org/10.4401/ag-3723>

- Yuan, S., Gessele, K., Gabriel, A.-A., May, D. A., Wassermann, J., and Igel, H., 2021. Seismic source tracking with six degree-of-freedom ground motion observations. *J. Geophys. Res.: Solid Earth*, **126**, e2020JB021112. <https://doi.org/10.1029/2020JB021112>.
- Yuan, S., Simonelli, A., Lin, C.-J., Bernauer, F., Donner, S., Braun, T., Wassermann, J., and Igel, H., 2020. Six Degree-of-Freedom Broadband Ground- Motion Observations with Portable Sensors: Validation, Local Earthquakes, and Signal Processing, *Bull. Seismol. Soc. Am.* **110**, 953 –969, doi: 10.1785/0120190277.

Authors Statement

Author Contributions: All authors have read and agreed to the revised version of the manuscript. Conceptualization and field work by JW, TB, MR, FG. Software and visualization by JW, FB; Investigation and Writing by all authors.

Journal Pre-proof

Declaration of interests

☐ The authors declare that they have no known competing financial interests or personal relationships that could have appeared to influence the work reported in this paper.

☒ The authors declare the following financial interests/personal relationships which may be considered as potential competing interests:

The third rotational motion sensor used in this study was lent to us by iXblue for the duration of the field experiment for free. Despite of this advantage no further financial interests or personal relationship of are or were existing.

Highlights:

- First six-degree-of-freedom measurements with a network of rotational motion sensors at an active volcano
- Identification of three visually different types of explosion quakes at Stromboli
- Localization of volcanic sources using the concepts of six-component polarization analysis
- Synthetics and real data reveal complex wave field in the near field of a volcanic source